J|A|C|S
ARTICLES

Published on Web 06/04/2010

Synthesis, Crystal and Electronic Structures of New Narrow-Band-Gap Semiconducting Antimonide Oxides RE_3SbO_3 and $RE_8Sb_{3-\delta}O_8$, with RE = La, Sm, Gd, and Ho

Peng Wang,[†] Scott Forbes,[†] Taras Kolodiazhnyi,[‡] Kosuke Kosuda,[§] and Yurij Mozharivskyj*,[†]

Department of Chemistry, McMaster University, 1280 Main Street West, Hamilton, Ontario L8S 4M1, Canada, and New Materials Group and Materials Analysis Station, National Institute for Materials Science, 1-1 Namiki, Tsukuba, Ibaraki 305-0044, Japan

Received April 12, 2010; E-mail: mozhar@mcmaster.ca

Abstract: In the search for high-temperature thermoelectric materials, two families of novel, narrow-band-gap semiconducting antimonide oxides with the compositions RE_3SbO_3 and $RE_8Sb_{3-\delta}O_8$ (RE = La, Sm, Gd, Ho) have been discovered. Their synthesis was motivated by attempts to open a band gap in the semimetallic RESb binaries through a chemical fusion of RESb and corresponding insulating RE_2O_3. Temperatures of 1350 °C or higher are required to obtain these phases. Both RE_3SbO_3 and $RE_8Sb_{3-\delta}O_8$ adopt new monoclinic structures with the $C2/m$ space group and feature similar REO frameworks composed of "RE_4O" tetrahedral units. In both structures, the Sb atoms occupy the empty channels within the REO sublattice. High-purity bulk Sm and Ho samples were prepared and subjected to electrical resistivity measurements. Both the RE_3SbO_3 and $RE_8Sb_{3-\delta}O_8$ (RE = Sm, Ho) phases exhibit a semiconductor-type electrical behavior. While a small band gap in RE_3SbO_3 results from the separation of the valence and conduction bands, a band gap in $RE_8Sb_{3-\delta}O_8$ appears to result from the Anderson localization of electrons. The relationship among the composition, crystal structures, and electrical resistivity is analyzed using electronic structure calculations.

Introduction

Thermoelectric materials are able to perform cooling or heating when electrical current is applied (Peltier effect) or to generate voltage under a temperature gradient (Seebeck effect).[1] Thermoelectric devices offer many advantages over competing technologies in terms of durability, reliability, and ease of use. The limitation of current thermoelectric materials is their efficiency. A good thermoelectric material has to have a large Seebeck coefficient α and low thermal conductivity κ, while retaining a high electrical conductivity σ.[2] Narrow-band-gap semiconductors are favored for thermoelectric applications, as they offer optimized thermopower α and electrical conductivity σ.[3,4]

Different strategies have been employed to reduce lattice thermal conductivity in order to achieve higher thermoelectric efficiency. Generally, commercial thermoelectric materials like Bi_2Te_3-based materials[5,6] are composed of heavy elements which decrease lattice thermal vibrations.[4] Complex crystal structures, such as that of $Yb_{14}MnSb_{11}$,[7] can also be used to minimize thermal conductivity, since the efficiency of phonon propagation is inversely related to the number of atoms in the unit cell.[4] Furthermore, atomic partial occupancy and structure defects in some systems, for instance in "β-Zn_4Sb_3",[8,9] have been shown to disturb phonon propagation. As a result, such materials exhibit low thermal conductivity similar to that of glasses while maintaining the electrical conductivity of a crystalline solid.[4]

Rare-earth (RE) monoantimonides may be of particular interest for thermoelectric applications, as they contain some of the heaviest elements in the periodic table. However, these phases adopt a simple NaCl-type crystal structure and are expected to possess a relatively high thermal conductivity due to the small number of atoms in their unit cells,[10,11] and thus some structural modifications will be required to make them competitive. Additionally, the RESb binaries exhibit large thermal stabilities due to the strong RE−Sb bonds present in the NaCl-type structure; most of the RESb binaries melt above

---

[†] Department of Chemistry, McMaster University.

[‡] New Materials Group, NIMS, Japan.

[§] Materials Analysis Station, NIMS, Japan.

(1) Tritt, T. M. *Science* **1996**, *272*, 1276–1277.

(2) Disalvo, F. J. *Science* **1999**, *285*, 703–706.

(3) Rowe, D. M. In *Thermoelectrics Handbook—Macro to Nano*; Rowe, D. M., Ed.; CRC Press: Boca Raton, FL, 2006; pp 1−8.

(4) Slack, G. A. In *CRC Handbook of Thermoelectrics*; Rowe, D. M., Ed.; CRC Press: Boca Raton, FL, 1995.

(5) Scherrer, S. S. In *Thermoelectrics Handbook—Macro to Nano*; Rowe, D. M., Ed.; CRC Press: Boca Raton, FL, 2006; pp 27−31.

(6) Satterthwaite, C. B.; Ure, R. W., Jr. *Phys. Rev.* **1957**, *108*, 1164–1170.

(7) Brown, S. R.; Kauzlarich, S. M.; Gascoin, F.; Snyder, G. J. *Chem. Mater.* **2006**, *18*, 1873–1877.

(8) Mozharivskyj, Y.; Pecharsky, A. O.; Bud'ko, S.; Miller, G. J. *Chem. Mater.* **2004**, *16*, 1580–1589.

(9) Nylen, J.; Andersson, M.; Lidin, S.; Haeussermann, U. *J. Am. Chem. Soc.* **2004**, *126*, 16306–16307.

(10) Nolas, G. S.; Cohn, J. L.; Chakoumakos, B. C.; Slack, G. A. *Therm. Conduct.* **2000**, *25*, 122–129.

(11) Gaume, R.; Viana, B.; Vivien, D.; Roger, J.-P.; Fournier, D. *Appl. Phys. Lett.* **2003**, *83*, 1355–1357.

10.1021/ja1027698 © 2010 American Chemical Society

2000 °C.[12] Thus, there is potential for using them or their derivatives for high-temperature applications. In terms of the electronic properties, RE monoantimonides are semimetallic compounds[13] in which the bottom of the conduction band and the top of the valence band are situated in different parts of the momentum space (at different k vectors), resulting in a "negative" indirect band gap.[14] Because of this feature, the pristine binaries are unsuitable for thermoelectric applications, as their metallic-type electronic structures compromise their thermopower.[12,14] In order for the RESb phases or their derivatives to be competitive, both their electronic and thermal properties have to be optimized. One of the possible chemical approaches to produce narrow-band-gap semiconductors from the RESb binaries is to combine them with electrically insulating rare-earth oxides, RE_2O_3. One can argue that strong interactions between the oxygen and RE atoms will push up the conduction band, composed primarily of the antibonding RE states, and thus will open a band gap. The thermal conductivity of the resulting phases is expected to be reduced due to an increased structural complexity. Also, the new phases may be thermally stable, as the strong RE−Sb and RE−O bonds will be transferred into their structures.

Chemical combinations of RE, Sb, and O have been tried before and led to the discovery of the $RE_3Sb_5O_{12}$ and RE_3SbO_7 oxides[15−17] and $RE_9Sb_5O_5$ antimonide oxides.[18−20] The fully oxidized $RE_3Sb_5O_{12}$ and RE_3SbO_7 phases are unsatisfactory for thermoelectric applications, as they are electrical insulators (their band gaps are wide). The $RE_9Sb_5O_5$ antimonide oxides are metallic due to the presence of conduction electrons ($RE^{3+}{}_9Sb^{3-}{}_5O^{2-}{}_5(2e^-)$) and thus are also unsuitable. However, the $RE_9Sb_5O_5$ structures are quite interesting, as they contain NaCl-type RESb slabs that are sandwiched between the "RE_4O_5" layers.[18−20] The discovery of the $RE_9Sb_5O_5$ phases suggests that it is possible to chemically fuse RESb and RE_2O_3 binaries to obtain novel antimonide oxides.

Considering the high thermal stabilities of the RESb and RE_2O_3 binaries, we explored high-temperature synthetic routes for new antimonide oxides through direct combination of RESb and RE_2O_3. During such studies, we have discovered novel phases with the RE_3SbO_3 and $RE_8Sb_{3-\delta}O_8$ compositions (RE = La, Sm, Gd, Ho). This work describes the preparation, characterization, and electronic structure investigation as well as some electrical properties of these new compounds.

Experimental Section

Synthesis. The starting materials were pieces of RE metals (99.99 wt %, SmartElements) and antimony (99.999 wt %, CERAC Inc.) and RE_2O_3 powders (99.999 wt %, Rhône-Poulenc). As the first step, RESb binaries were prepared by direct sintering of the elements. Mixtures of the RE metal filings and ground antimony in a 1:1 atomic ratio were pressed into 1 g pellets in a glovebox. The samples were sealed in evacuated silica tubes 10−15 cm in length and then heated to 600 °C at a rate of 50 °C/h. The sintering temperature was maintained at 600 °C to allow antimony to react with a RE. After 12 h, the temperature was raised to 850 °C at 50 °C/h and held for 48 h to drive the reaction to completion. Black pellets were obtained after cooling in air. The purity of these binaries was confirmed by X-ray powder analysis.

Table 1. Optimal Synthetic Conditions for the RE_3SbO_3 and $RE_8Sb_3O_8$ Samples

phase	treatment 1	treatment 2	sample description
La_3SbO_3	2 h at 1350 °C	–	dark silver solidified pieces
$La_8Sb_3O_8$	6 h at 1350 °C	–	dark silver solidified pieces
Sm_3SbO_3	2 h at 1600 °C	2 h at 1600 °C	dark silver solidified pieces
$Sm_8Sb_3O_8$	6 h at 1500 °C	6 h at 1350 °C	dark gray pellets
Gd_3SbO_3	0.5 h at 1600 °C	0.5 h at 1600 °C	dark gray pellets
$Gd_8Sb_3O_8$	6 h at 1500 °C	6 h at 1500 °C	dark gray pellets
Ho_3SbO_3	1 h at 1600 °C	1 h at 1600 °C	dark gray pellets
$Ho_8Sb_3O_8$	6 h at 1600 °C	6 h at 1500 °C	dark gray pellets

The ground RE monoantimonides were mixed with RE_2O_3 in a 1:1 molar ratio to prepare the RE_3SbO_3 samples, and with RE_2O_3 and Sb in a 8:8:1 ratio for $RE_8Sb_3O_8$ samples. The powders were thoroughly mixed and pressed into 0.5 g pellets in a glovebox. The pellets were sealed in tantalum tubes under an argon atmosphere. The Ta tubes were placed into a molybdenum susceptor and heated in a high-frequency induction furnace under dynamic vacuum below 10^{-5} Torr. The reaction temperature was monitored by an optical pyrometer. The RE_3SbO_3 and $RE_8Sb_3O_8$ samples were heated between 1300 and 1600 °C. To ensure homogeneity, after the first annealing each sample was ground and pressed in a glovebox, sealed in a fresh tantalum tube, and heat-treated again. At the end of each heat treatment, the samples were left to cool to room temperature under dynamic vacuum. The final products were either molten or sintered into solid pellets. A variety of temperatures and annealing times have been tested, and the optimal synthetic conditions for each phase are listed in Table 1.

X-ray Single-Crystal Diffraction and Structure Refinement. X-ray single-crystal diffraction studies were performed on crystals extracted from the crushed RE_3SbO_3 and $RE_8Sb_3O_8$ samples (RE = La, Sm, Gd, Ho). Room-temperature diffraction data were collected on a STOE IPDSII diffractometer with Mo Kα radiation in the whole reciprocal sphere. A numerical absorption correction was based on the crystal shape that was originally derived from the optical face indexing but was later optimized against equivalent reflections using the STOE X-Shape software.[21] The data for the $Ho_8Sb_3O_8$ single crystal were also collected on a Bruker SMART Apex II CCD diffractometer (Mo Kα radiation) at 100(2) K in a reciprocal hemisphere. Intensities were extracted and then corrected for Lorentz and polarization effects through the SAINT program.[22] Numerical absorption correction was based on the crystal shape obtained from the optical face indexing. Due to the poor crystal quality, the $La_8Sb_3O_8$ structure could not be refined from the corresponding X-ray data; only the unit cell parameters were obtained from indexing of the Braggs peaks. Structural determinations and refinements were performed using the SHELXL program.[23] Both the RE_3SbO_3 and $RE_8Sb_3O_8$ structures adopt the $C2/m$ space group. The crystallographic and structural information for Ho_3SbO_3 and $Ho_8Sb_3O_8$ is summarized in Tables 2 and 3, detailed refinement results (including those for other RE antimonide oxides) are given in the Supporting Information.

Within the initial structural solution for the $RE_8Sb_3O_8$ crystals, Sb2 atoms were placed on the $2a$ site (0,0,0) with the $2/m$ symmetry. However, unusually large vibrations along the b direction suggested that the Sb2 atoms have to be moved out of the mirror plane into

---

(12) Abdusalyamova, M. N.; Shokirov, H. S.; Rakhmatov, O. I. *J. Less-Common Met.* **1990**, *166*, 221–227.

(13) Li, D. X.; Haga, Y.; Shida, H.; Suzuki, T.; Kwon, Y. S. *Phys. Rev. B: Condens. Matter Mater. Phys.* **1996**, *54*, 10483–10491.

(14) Larson, P.; Lambrecht, W. R. L. *Phys. Rev. B: Condens. Matter Mater. Phys.* **2006**, *74*, 085108/1−9.

(15) Fennell, T.; Bramwell, S. T.; Green, M. A. *Can. J. Phys.* **2001**, *79*, 1415–1419.

(16) Hinatsu, Y.; Ebisawa, H.; Doi, Y. *J. Solid State Chem.* **2009**, *182*, 1694–1699.

(17) Marcano, C. M.; Rasines, I. *Inorg. Chim. Acta* **1985**, *109*, L15–L16.

(18) Nuss, J.; Jansen, M. *Acta Crystallogr. B* **2007**, *B63*, 843–849.

(19) Nuss, J.; Jansen, M. *Z. Kristallogr. New Cryst. Struct.* **2009**, *224*, 11–12.

(20) Nuss, J.; von Schnering, H. G.; Grin, Y. *Z. Anorg. Allg. Chem.* **2004**, *630*, 2287–2291.

(21) *STOE X-Shape*; STOE & Cie GmbH: Darmstadt, Germany, 2004.

(22) *SAINT*; Bruker Analytical X-ray Systems: Madison, WI, 2002.

(23) Sheldrick, G. M. *SHELXL*; University of Gottingen, Germany, 1997.

Table 2. Crystallographic Data and Refinement Results for the Single Crystals from the Ho_3SbO_3 and $Ho_8Sb_3O_8$ Samples

	Ho_3SbO_3	$Ho_8Sb_3O_8$	$Ho_8Sb_3O_8$
refined composition	Ho_3SbO_3	$Ho_8Sb_{2.950(8)}O_8$	$Ho_8Sb_{2.946(4)}O_8$
temperature, K	293(2)	293(2) K	100(2) K
space group	$C2/m$	$C2/m$	$C2/m$
unit cell dimensions	$a = 13.014(3)$ Å $b = 3.8218(7)$ Å $c = 11.680(2)$ Å $\beta = 118.21(1)°$	$a = 13.137(1)$ Å $b = 3.7609(2)$ Å $c = 14.870(1)$ Å $\beta = 106.958(7)°$	$a = 13.145(2)$ Å $b = 3.7597(5)$ Å $c = 14.874(2)$ Å $\beta = 107.025(5)°$
volume, Å^3	511.90(2)	702.73(9)	702.90(2)
Z	4	2	2
goodness-of-fit on F^2	0.914	1.015	1.040
final R indices [$I > 2\sigma(I)$]	$R_1 = 0.0518$, $wR_2 = 0.0788$	$R_1 = 0.0410$, $wR_2 = 0.0660$	$R_1 = 0.0353$, $wR_2 = 0.0666$
R indices (all data)	$R_1 = 0.1185$, $wR_2 = 0.0943$	$R_1 = 0.0737$, $wR_2 = 0.0720$	$R_1 = 0.0467$, $wR_2 = 0.0705$

Table 3. Atomic and Equivalent Isotropic Temperature (U) Parameters for the Single Crystals from the Ho_3SbO_3 and $Ho_8Sb_3O_8$ Samples

atom	site	occupancy	x	y	z	U (Å^2)
			Ho_3SbO_3 (293 K)			
Ho(1)	4i	1	0.11994(8)	0	0.4433(1)	0.0079(2)
Ho(2)	4i	1	0.34264(8)	0	0.79342(9)	0.0077(2)
Ho(3)	4i	1	0.87230(8)	0	0.09852(9)	0.0092(2)
Sb(1)	4i	1	0.3820(1)	0	0.3190(2)	0.0094(2)
O(1)	4i	1	0.313(1)	0	0.592(1)	0.007(2)
O(2)	4i	1	0.334(1)	0	0.983(1)	0.014(3)
O(3)	4i	1	0.935(1)	0	0.807(1)	0.014(3)
			$Ho_8Sb_3O_8$ (293 K)			
Ho(1)	4i	1	0.71926(4)	0	0.08908(4)	0.0072(1)
Ho(2)	4i	1	0.45628(4)	0	0.16929(4)	0.0111(1)
Ho(3)	4i	1	0.87741(4)	0	0.34761(4)	0.0074(1)
Ho(4)	4i	1	0.64347(4)	0	0.43042(4)	0.0086(1)
Sb(1)	4i	1	0.17137(6)	0	0.26664(6)	0.0130(2)
Sb(2)	4g	0.475(4)	0	0.050(1)	0	0.012(1)
O(1)	4i	1	0.4691(6)	0	0.3688(9)	0.023(2)
O(2)	4i	1	0.8826(7)	0	0.2018(5)	0.010(2)
O(3)	4i	1	0.2960(6)	0	0.0663(6)	0.008(1)
O(4)	4i	1	0.1649(6)	0	0.5144(6)	0.009(1)
			$Ho_8Sb_3O_8$ (100 K)			
Ho(1)	4i	1	0.71909(2)	0	0.08906(2)	0.00385(5)
Ho(2)	4i	1	0.45656(2)	0	0.16947(2)	0.00700(6)
Ho(3)	4i	1	0.87733(2)	0	0.34747(2)	0.00408(5)
Ho(4)	4i	1	0.64392(2)	0	0.42967(2)	0.00499(5)
Sb(1)	4i	1	0.17149(3)	0	0.26621(3)	0.00909(8)
Sb(2)	4g	0.473(2)	0	0.0516(3)	0	0.0084(3)
O(1)	4i	1	0.4708(4)	0	0.3689(5)	0.013(1)
O(2)	4i	1	0.8833(4)	0	0.2024(3)	0.0055(7)
O(3)	4i	1	0.2966(4)	0	0.0662(3)	0.0064(7)
O(4)	4i	1	0.1663(4)	0	0.5151(4)	0.0072(7)

Table 4. Effects of Moving the Sb2 Atom from the 2a Site ($y = 0$) into the 4g Site ($y \neq 0$) and Refining Its Occupancy on the Thermal Parameters and R_1 Values for the $Ho_8Sb_3O_8$ Crystal

temp (K)	Sb2 site	occupancy	y	U_{22}	U_{eq}	R_1 value
293	2a	1.0	0.0	0.066(1)	0.0293(4)	0.0417
293	4g	0.5	0.050(1)	0.024(3)	0.0156(9)	0.0413
293	4g	0.475(4)	0.050(1)	0.018(2)	0.012(1)	0.0410
100	2a	1.0	0.0	0.0592(7)	0.0234(2)	0.0399
100	4g	0.5	0.0516(3)	0.020(1)	0.0106(3)	0.0360
100	4g	0.473(2)	0.0516(3)	0.0166(9)	0.0084(3)	0.0353

the 4g site (0,y,0) with the occupancy of 50%. While split positions can indicate the presence of a superstructure, we saw no signs of a superstructure in the reciprocal spaces of $RE_8Sb_3O_8$. The 50% occupancy provides the right number of atoms in the unit cell and accounts for artificially short Sb2−Sb2 distances of ca. 0.4 Å. The new structural model yielded improved thermal parameters for the Sb2 sites and lower R values (Table 4 and Supporting Information). In addition, the Sb2 site is refined to be deficient. Upon releasing the Sb2 occupancies, the R factors were either preserved or improved, while the thermal vibration parameters of Sb2 atoms were further reduced (Table 4 and Supporting Information). The most pronounced Sb2 deficiency was observed for $Ho_8Sb_3O_8$. During the refinement, atomic deficiencies and temperature factors are usually correlated; however, they can be untangled from the high-angle diffraction data, as their contribution to the structure amplitudes is different at high angles. Additionally, lower temperatures decrease thermal vibrations and allow further differentiation of the two effects. The single-crystal data for $Ho_8Sb_3O_8$ were recollected up to $2\theta = 90°$ and at 100 K, and they confirmed both the deficiency for and the assignment of the 4g site to the Sb2 atoms. Therefore, the composition of the $RE_8Sb_3O_8$ phases is given as $RE_8Sb_{3-\delta}O_8$.

The bonding aspects of the new structural model and its correlation with electrical resistivity are analyzed in depth later in this work. Further details of the crystal structure investigations can be obtained from the Fachinformationszentrum Karlsruhe, 76344 Eggenstein-Leopoldshafen, Germany (fax (49) 7247-808-666; e-mail crysdata@fiz.karlsruhe.de), by quoting the CSD depository numbers 380456 for La_3SbO_3, 380455 for Sm_3SbO_3, 380454 for $Sm_8Sb_{3-\delta}O_8$, 380460 for Gd_3SbO_3, 380459 for $Gd_8Sb_{3-\delta}O_8$, 380458 for Ho_3SbO_3, and 380457 for $Ho_8Sb_{3-\delta}O_8$; these details are also provided as Supporting Information.

X-ray Powder Diffraction. The sintered samples were subjected to X-ray powder diffraction analysis to assess their purity, derive lattice constants, and understand the transformation pathways between the RE_3SbO_3 and $RE_8Sb_{3-\delta}O_8$ phases. Between 20 and 50 mg of sample was used for each data collection. Diffraction data in the 20−70° 2θ range were collected on a PANalytical X'Pert Pro diffractometer with an X'Celerator detector and Cu Kα_1 radiation. The full-profile Rietveld refinement (Rietica program[24]) was used to refine the lattice constants and amount of impurities. The structural models obtained from X-ray single-crystal diffraction were used during the Rietveld refinement. The lattice constants and phase analysis of the samples are provided in the Supporting Information.

Energy-Dispersive X-ray Spectroscopy. In order to verify the sample compositions and test for possible contamination, bulk samples and single crystals of the phases prepared were analyzed by energy-dispersive X-ray spectroscopy (EDS). The EDS experiments were conducted on a JEOL 7000F scanning electron microscope. Copper metal was used to standardize the signals. Qualitative information obtained from experiments was in agreement with the X-ray single-crystal and powder diffraction results. No contamination, including Ta impurities, was observed in the RE_3SbO_3 and $RE_8Sb_3O_8$ samples.

Microprobe Analysis. Quantitative elemental analysis of the Sm- and Ho-containing samples was performed by electron probe microanalysis (EPMA) using wavelength-dispersive (WDS) X-ray spectroscopy (model JXA-8500F, JEOL). Samples were mounted in an epoxy resin 1 in. in diameter and 10 mm in thickness. Diamond dust, ~10 μm, was used during the final polishing stage. Antimony metal, $Sm_3Ga_5O_{12}$, and HoP_5O_{14} were used as standards to determine the concentration of Sb, Ho, Sm, and O in the RE_3SbO_3 and $RE_8Sb_3O_8$ samples.

Physical Property Measurements. Four-probe direct current electrical resistivity of the Sm- and Ho-containing samples was measured on a Quantum Design Physical Properties Measurement System in the temperature interval of 2−300 K. Gold wires of 50 μm diameter were attached to the samples using silver ink. Due to the irregular shape of the samples, the *Y*-axis error bars in Figure 7 (below) correspond to around 30% of the absolute value of electrical resistivity. Quite often, the high resistivity of the polycrystalline samples originates from the scattering of the charge carriers on the grain boundaries. This effect cannot be distinguished by the direct current measurements.[25] To confirm that the resistivity at low temperatures is not attributed to the grain boundaries but is a true bulk property of the samples, we performed complex impedance analysis of the $Ho_8Sb_3O_8$ sample at 3−300 K and alternating current frequency range of 10^2 -20^6 Hz using an Agilent E4980 Precision LCR meter. We found no evidence of the grain boundary effect and confirm, therefore, that the reported resistivity is characteristic of the bulk of the material.

Electronic Structure Calculations. Tight-binding, linear-muffin-tin orbital calculations using the atomic sphere approximation (TB-LMTO-ASA)[26] were performed for Ho_3SbO_3 and $Ho_8Sb_3O_8$ with the Stuttgart program.[27] The single-crystal lattice and atomic parameters were used during calculations. For $Ho_8Sb_3O_8$, two structural models were used: one with the Sb2 atoms on the 2*a* site and the other with the Sb2 atoms on the 4*g* site. In the latter case, the symmetry was reduced to P2, and a superstructure was created (Figure 3, below). The Ho f-electrons were treated as core electrons due to their localized nature. This approach produces reliable density of states (DOS) and COHP results, provided magnetic interactions are not of interest.[28] In our case, the Ho_3SbO_3 and $Ho_8Sb_{3-\delta}O_8$ phases are paramagnetic at room temperature; therefore, magnetic interactions are not considered. Exchange and correlation were treated by the local density approximation (LDA).[29] All relativistic effects except spin−orbit coupling were taken into account by using a scalar relativistic approximation.[30] In the ASA method, space is filled with overlapping Wigner−Seitz (WS) atomic spheres, the radii of which were obtained by requiring the overlapping potential to be the best possible approximation to the full potential. To satisfy the overlap criteria of the atomic spheres in the TB-LMTO-ASA method, empty spheres were included in the unit cell, employing automatic sphere generation.[31]

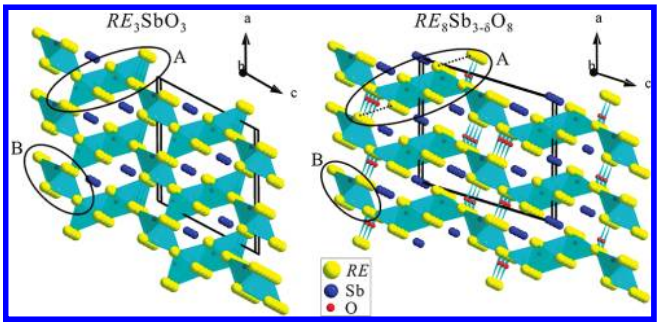

Figure 1. Crystal structures of the RE_3SbO_3 and $RE_8Sb_{3-\delta}O_8$ phases and their building blocks.

Results and Discussion

Structures. The RE_3SbO_3 and $RE_8Sb_{3-\delta}O_8$ antimonide oxides adopt novel crystal structures with *C*2/*m* symmetry (Figure 1). The two structures feature similar REO frameworks built from the RE_4O edge-sharing tetrahedra. Also, in both structures the empty channels running along the *b* direction are filled with Sb atoms. There are two types of building blocks, A and B, in the REO framework of RE_3SbO_3 (Figure 1, left). Block A consists of four edge-sharing RE_4O tetrahedra and block B of two such tetrahedra. The two types of blocks, connected via corner-sharing, form a 2D slab within the *ac* plane. These slabs stack along the *b* axis via edge-sharing and form the 3D REO framework. The empty channels within the REO framework of RE_3SbO_3 are occupied by two rows of Sb atoms.

Compositionally, the RE_3SbO_3 phases are direct combinations of the RESb and RE_2O_3 binaries. Thus, it is interesting to see if there are any structural similarities between them. Indeed, the RE_4O tetrahedra, which define the REO framework of RE_3SbO_3, are also found in RE_2O_3; in fact, the entire framework of the *C*-type RE_2O_3 oxides is built from the edge-sharing RE_4O tetrahedra.[32] However, the RE cubic environment of the Sb atoms in RE_3SbO_3 is different from the RE octahedral environment of the Sb atoms in the NaCl-type RESb binaries.[12] This new coordination for Sb can be viewed as a structural adaptation of the Sb atoms (and Sb−Ho interactions) to the presence of

---

(24) Hunter, B. A.; Howard, C. J. *Rietica*; Australian Nuclear Science and Technology Organization: Menai, Australia, 2000.

(25) Kolodiazhnyi, T.; Petric, A. *J. Am. Ceram. Soc.* **2003**, *86*, 1554–1559.

(26) Andersen, O. K.; Pawlowska, Z.; Jepsen, O. *Phys. Rev. B: Condens. Matter Mater. Phys.* **1986**, *34*, 5253–69.

(27) Jepsen, O.; Burkhardt, A.; Andersen, O. K. *The TB-LMTO-ASA Program*, version 4.7; Max-Planck-Institut für Festkörperforschung: Stuttgart, Germany, 1999.

(28) Bobev, S.; Bauer, E. D.; Thompson, J. D.; Sarrao, J. L.; Miller, G. J.; Eck, B.; Dronskowski, R. *J. Solid State Chem.* **2004**, *177*, 3545–3552.

(29) Andersen, O. K.; Jepsen, O. *Phys. Rev. Lett.* **1984**, *53*, 2571–4.

(30) Andersen, O. K.; Jepsen, O.; Glotzel, D. In *Highlights of Condensed-Matter Theory*; Bassani, F., Fumi, F., Tosi, M. P., Eds.; Elsevier: Amsterdam, 1985.

(31) Jepsen, O.; Andersen, O. K. *Z. Phys. B: Condens. Matter* **1995**, *97*, 35–47.

(32) Sarbak, Z. In *Binary Rare Earth Oxides*; Adachi, G., Imanaka, N., Kang, Z. C., Eds.; Kluwer Academic Publishers: Dordrecht, 2004; Vol. 84.

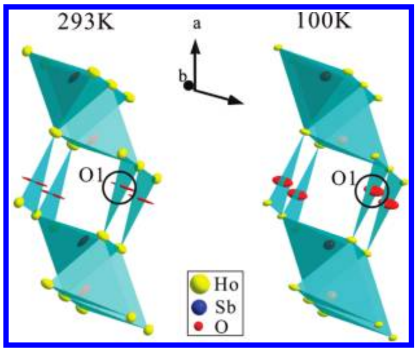

Figure 2. Thermal vibrations (90% probability) of O1 in $Ho_8Sb_{3-\delta}O_8$.

the REO framework. Similar structural relationships are observed among $RE_8Sb_{3-\delta}O_8$, RESb, and RE_2O_3.

In the $RE_8Sb_{3-\delta}O_8$ structure, building block B of RE_3SbO_3 is retained (Figure 1, right), but block A is expanded with two additional, highly distorted RE_4O tetrahedra. For example, in $Ho_8Sb_{3-\delta}O_8$, the longest Ho−Ho distance (a dotted line in Figure 1) in these distorted tetrahedra is 3.94(2) Å, while the five other distances are within the 3.80−3.84 Å range. In addition to being strongly stretched, these RE_4O units have oxygen atoms (the O1 site) almost in the center of their terminal triangular faces. As the result, the O1 atoms adopt a rather unusual, trigonal planar environment: for example, in $Ho_8Sb_{3-\delta}O_8$, the O1 atoms have three Ho atoms at 2.19−2.22 Å and a fourth one at 2.92 Å. Similar oxygen shifts are also observed for the terminal RE_4O tetrahedra of the A block in RE_3SbO_3, but they are less pronounced; for example, in Ho_3SbO_3, the O atoms (the O3 site) have three Ho atoms at 2.21−2.23 Å and a fourth one at 2.66 Å. The unusual coordination for the O1 atoms in $RE_8Sb_{3-\delta}O_8$ and the absence of strong interactions outside of the RE trigonal face manifest themselves in the displacement parameters that are highly elongated along the normal to the face (Figure 2). The presence of elongated thermal ellipsoids at 100 K, similar to the room-temperature ones (Figure 2), further supports the argument that the origin of these vibrations lies in the unusual environment of the O1 atoms.

The extended A blocks of $RE_8Sb_{3-\delta}O_8$ create larger channels which are now occupied by three rows of Sb atoms (only two such rows are present in RE_3SbO_3). Conversely, it can be also argued that the extra Sb row in $RE_8Sb_{3-\delta}O_8$ puts additional pressure on the dimension of the A block, which results not only in the extension of this block by two RE_4O tetrahedra but also in the stretching of the terminal RE_4O tetrahedra and thus unusual bonding environment for the O1 atoms. While block A is larger in $RE_8Sb_{3-\delta}O_8$, the connectivity between and stacking of blocks A and B are identical to those in RE_3SbO_3.

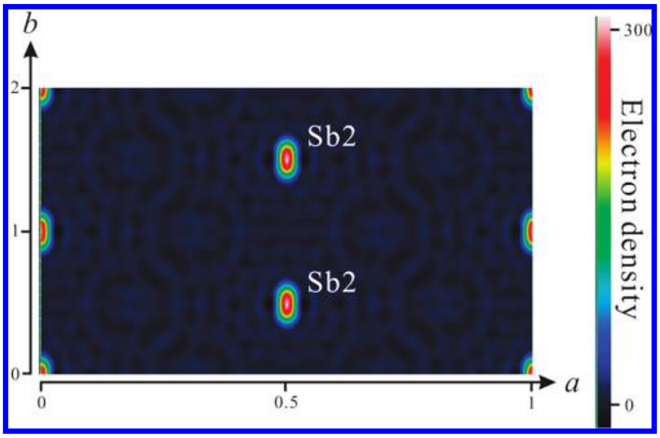

Figure 4. Experimental electron density map for the $Ho_8Sb_3O_8$ single crystal at $z = 0$ and 100 K.

Another interesting structural feature of $RE_8Sb_{3-\delta}O_8$ is anisotropic thermal vibrations and positions of the Sb2 atoms (the central row of Sb atoms) along the *b* direction. In the original structure model with the Sb2 atoms on the mirror plane (model 1 in Figure 3), the Sb2−Sb2 distances equaled the *b* parameter and were identical to the Sb1−Sb1 distances. However, the thermal vibrations of Sb2 were found to be extremely elongated along the *b* direction and much larger than those of the Sb1 atoms, despite the fact that the atomic environments of Sb1 and Sb2 were rather similar. Furthermore, the electron density map generated from the experimental intensities showed that the Sb2 site has a large spatial distribution along the *b* direction (Figure 4). In order to account for such smeared electron density, the Sb1 atoms were shifted from the mirror plane: from the 2*a* site (0,0,0) into the 4*g* site (0,*y*,0) (model 2 in Figure 3). The occupancy of the new site was set to 50% to avoid overlap between the Sb2 atoms, but after the refinement it became even lower (e.g., 47.3(2)% for $Ho_8Sb_{3-\delta}O_8$ at 100 K). The distribution of Sb2 above and below the mirror plane appears to be random, as no superstructure could be detected, and also static, as the refinements of the room-temperature and 100 K data yielded identical structural models.

The Sb2 shifts in $RE_8Sb_{3-\delta}O_8$ result in unequal Sb2−Sb2 distances along the *b* direction. Such distances can be visualized through the construction of a superstructure ("Model 2 Superstructure" in Figure 3), in which the *b* axis is doubled and half of the Sb2 atoms are removed. As mentioned above, no evidence for such a superstructure could be detected from single-crystal experiments. There are two distinct sets of the Sb2−Sb2 distances: longer ones of 4.148(1) Å and shorter ones of 3.371(1) Å. While the shorter distances are longer than a typical single Sb−Sb bond (e.g., $d_{Sb-Sb} = 2.83-2.85$ Å in KSb[33]), they are indicative of increased Sb2−Sb2 interactions and, thus, of the formation of Sb2−Sb2 bonds which can be treated as elongated dimers. A similar behavior has been also observed in

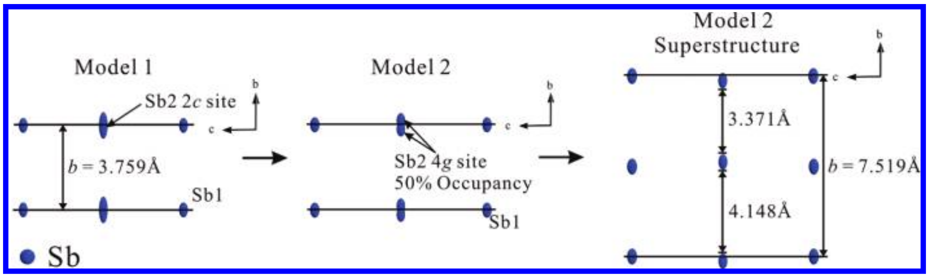

Figure 3. Models with different Sb2 positions used for the structural refinements of the $RE_8Sb_3O_8$ single crystal. The superstructure model was employed for the linear-muffin-tin orbital calculations. The thermal ellipsoids are shown with 90% probability.

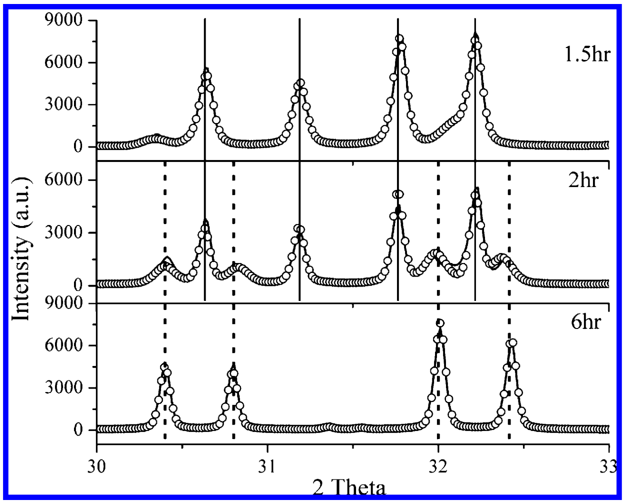

Figure 5. X-ray powder diffraction patterns of the Ho_3SbO_3 samples after 1.5, 2, and 6 h of annealing at 1600 °C. Dashed lines mark the peak positions of the Ho_3SbO_3 phase, and solid lines mark the peak positions of the $Ho_8Sb_{3-\delta}O_8$ phase.

$Yb_{14}MnSb_{11}$,[7] where a central Sb atom of the Sb_3 linear unit randomly shifts toward and form a dimer with one of the terminal Sb atoms.[34] Such random dimer formation is believed to be one of the key factors responsible for the low thermal conductivity and outstanding thermoelectric performance of $Yb_{14}MnSb_{11}$.[35]

It is worth noting that refinements of the Sb2 site for different $RE_8Sb_{3-\delta}O_8$ (RE = Sm, Gd, Ho) single crystals yielded occupancies smaller than 50%. Such deficiency does not appear to be a simple correction to the thermal motion of the atom, since the refinement on the 100 K data for $Ho_8Sb_{3-\delta}O_8$ yielded similar results. While the deficiencies are rather minor, they are statistically significant for the Gd and Ho structures, and according to the Hamilton test,[36] they should be accepted with a larger than 99.5% confidence level. It can be argued that formation and random distribution of the Sb2−Sb2 dimers is the cause for the Sb2 deficiencies. If all Sb2 atoms form dimers and no isolated Sb2 atoms are allowed, then a random distribution of the dimers can be achieved only if some of the Sb2 atoms are missing.

Stability and Transformation of the Antimonide Oxides. From the analysis of the products at different stages, we have observed that formation of RE_3SbO_3 always precedes the formation of $RE_8Sb_{3-\delta}O_8$, even if the loading composition is $RE_8Sb_3O_8$. Also, if one starts with the RE_3SbO_3 compositions, one obtains the RE_3SbO_3 phases first, which then transform into the $RE_8Sb_{3-\delta}O_8$ phases upon longer annealing. Figure 5 demonstrates conversion from Ho_3SbO_3 into $Ho_8Sb_{3-\delta}O_8$ as seen from X-ray powder diffraction. The loading composition of Ho_3SbO_3 yields the desired phase in high purity (>90%) after 1.5 h of heating at 1500 °C, accompanied only by small amounts of $Ho_8Sb_{3-\delta}O_8$. As the same loading composition is annealed for 2 h at the same temperature, the $Ho_8Sb_{3-\delta}O_8$ phase starts to grow at the expense of Ho_3SbO_3. After 6 h at 1500 °C, the Ho_3SbO_3 sample yields an almost pure $Ho_8Sb_3O_8$ phase. The same trends were observed for other systems. Since the total Sb deficiency is very small (the largest one is 1.8 at. % for $Ho_8Sb_{3-\delta}O_8$), synthesis of the $RE_8Sb_{3-\delta}O_8$ phases always proceeded from the $RE_8Sb_3O_8$ loading compositions.

Table 5. Composition of the RE_3SbO_3 and $RE_8Sb_3O_8$ Samples with RE = Sm, Ho from the Electron Microprobe Analysis[a]

	Ho_3SbO_3		Sm_3SbO_3		$Ho_8Sb_3O_8$		$Sm_8Sb_3O_8$	
element	at. %	ratio	at. %	ratio	at. %	ratio	at. %	ratio
RE	41.5(5)	3.03(4)	41.8(5)	2.88(3)	40.8(5)	8.4(1)	40.3(5)	8.1(1)
Sb	13.7(8)	1.00(6)	14.5(8)	1.00(6)	14.6(8)	3.0(2)	15.0(7)	3.0(1)
O	44.8(7)	3.27(5)	43.7(7)	3.01(5)	44.7(7)	9.2(1)	44.9(6)	9.0(1)

[a] The elemental ratios were normalized to three and eight Sb atoms.

Thus, the $RE_8Sb_{3-\delta}O_8$ phases appear to be thermodynamically more stable under our synthetic conditions. It has also been found that transformation of RE_3SbO_3 into $RE_8Sb_{3-\delta}O_8$ occurs more fully at lower temperatures. Taking advantage of different stabilities, synthetic routines were designed to produce either RE_3SbO_3 or $RE_8Sb_{3-\delta}O_8$ in high purity for Sm, Gd, and Ho. As summarized in Table 1, the RE_3SbO_3 phases can be obtained from shorter treatments at higher temperature and the $RE_8Sb_{3-\delta}O_8$ ones from longer annealing at lower temperatures. Regardless of the annealing temperature and duration, La_3SbO_3 and $La_8Sb_{3-\delta}O_8$ could be obtained only as mixtures.

The transformation and relative stability of RE_3SbO_3 and $RE_8Sb_{3-\delta}O_8$ can be explained considering their compositions and structures. Compositionally, the RE_3SbO_3 phases are direct combinations of the RESb and RE_2O_3 binaries, and their structures are simpler than those of $RE_8Sb_{3-\delta}O_8$. Thus, during synthesis, the RE_3SbO_3 phases appear first, but additional heat treatment permits further structural and compositional modifications toward the $RE_8Sb_{3-\delta}O_8$ phases. Since the $RE_8Sb_{3-\delta}O_8$ phases always appear as the final product, even in the RE_3SbO_3 samples, one may question their real compositions. To verify compositions, quantitative electron microprobe analysis was performed for the RE_3SbO_3 and $RE_8Sb_3O_8$ samples with RE = Sm, Ho. As summarized in Table 5, the RE:Sb ratios are significantly different for the RE_3SbO_3 and $RE_8Sb_3O_8$ samples (oxygen amounts have to be treated with caution as the surfaces are oxidized). Therefore, the RE_3SbO_3 and $RE_8Sb_{3-\delta}O_8$ phases do possess distinct chemical compositions; i.e., they are not structural polymorphs. Also, no impurities were detected in the samples.

The RE_3SbO_3 antimonide oxides transform into $RE_8Sb_{3-\delta}O_8$ upon prolonged annealing; however, byproducts of this reaction have never been detected in the bulk samples from the X-ray powder analysis. The "missing" byproducts were found during the SEM analysis of the tantalum ampule, in which Ho_3SbO_3 was allowed to convert into $Ho_8Sb_{3-\delta}O_8$. Small crystalline clusters about 5−10 μm in size were deposited uniformly on the inside surface of the Ta ampule (Figure 6). Energy-dispersive X-ray spectroscopy analysis of these clusters yielded only Ho and O as their constituents, but their exact ratio could not be determined accurately due to the bias in oxygen content. We believe that RE_2O_3 and RE metals precipitate out during the $RE_3SbO_3 \rightarrow RE_8Sb_{3-\delta}O_8$ transformation.

Electrical Resistivity. Electric resistivity measurements were performed on the Sm_3SbO_3, $Sm_8Sb_3O_8$, Ho_3SbO_3, and $Ho_8Sb_3O_8$ samples. As shown in Figure 7, an exponential decrease in electric resistivity indicative of a semiconducting-type behavior is observed for all samples. The room-temperature electrical resistivity and band gap values are listed in Table 6. The band gaps were calculated from the high-temperature data assuming an Arrhenius-type behavior and two types of charge carriers.

---

(33) Hoenle, W.; Von Schnering, H. G. *Z. Kristallogr.* **1981**, *155*, 307–314.
(34) Kleinke, H. *Inorg. Chem.* **1999**, *38*, 2931–2935.
(35) Kleinke, H.; Xu, J. *J. Comput. Chem.* **2008**, *29*, 2134–2143.
(36) Hamilton, W. C. *Acta Crystallogr.* **1965**, *18*, 502–510.

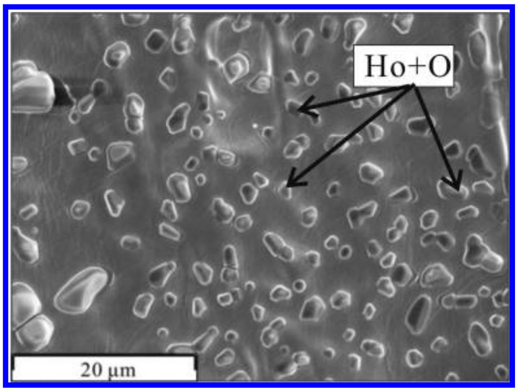

Figure 6. SEM image of the inside surface of the Ta ampule, in which Ho_3SbO_3 was converted into $Ho_8Sb_{3-\delta}O_8$.

In general, the Ho samples are more conductive that the Sm analogues, and the RE_3SbO_3 samples are more conductive than the $RE_8Sb_3O_8$ ones. Unfortunately, the room-temperature electrical resistivities for both the RE_3SbO_3 and $RE_8Sb_3O_8$ samples are 10^2-10^3 times larger than those of the high-performance thermoelectric materials (resistivity of $Yb_{14}MnSb_{11}$ and Zn_4Sb_3 is ~2 mΩ·cm for both at room temperature[7,37]). Such large resistivities render these phases in their current state unsuitable for thermoelectric applications.

Electronic Structure of RE_3SbO_3. Qualitatively, a semiconductor behavior of the RE_3SbO_3 phases can be explained using a simple electron-counting formalism. Since the RE atoms have no close RE neighbors, they can be treated as RE^{3+}. The Sb and O anions are assumed to satisfy the octet rule, and since there are no anion−anion interactions, the RE_3SbO_3 formula can be written as $RE_3{}^{3+}Sb^{3-}O_3{}^{2-}$. In terms of the electronic structure, such charge assignment would mean that the valence band composed primarily of the Sb states (O states will be lower) is fully occupied and the conduction band made primarily of the Ho states is empty. Obviously, an energetic separation between the two bands cannot be predicted from such a qualitative approach, but if a band gap is assumed, the RE_3SbO_3 phases will be semiconducting. These simple arguments are supported by the LMTO calculations for Ho_3SbO_3 (Figure 8). The calculated DOS exhibit a small band gap of 0.2 eV between the valence band dominated by the Sb p-orbitals and the conduction band formed primarily by Ho d-orbitals. The Fermi energy level resides at the top of the valence band, and Ho_3SbO_3 is predicted to be a small-band-gap semiconductor, which agrees with the experimental observations.

Electronic Structure of $RE_8Sb_{3-\delta}O_8$. Analysis of the electronic structure of the $RE_8Sb_{3-\delta}O_8$ phases is more complicated due to their increased structural complexity. For an idealized $RE_8Sb_3O_8$ structure (no Sb2 deficiencies and Sb2 on the 2*a* site; i.e., no Sb2−Sb2 dimers), the electron-counting approach yields a charge-*unbalanced* formula, $RE_8{}^{3+}Sb_3{}^{3-}O_8{}^{2-}$, and electron deficiency of $1e^-$. The Sb2 deficiency, δ, reduces the electron deficiency to $(1-3\delta)e^-$, but considering that experimental δ values are much smaller than 1/3, the $RE_8Sb_{3-\delta}O_8$ phases are predicted to be metallic. However, when all Sb2 atoms are assumed to form Sb2−Sb2 dimers (Sb2 on the 4*g* site), one obtains a $RE_8{}^{3+}Sb_2{}^{3-}Sb(2)^{2-}O_8{}^{2-}$ formula which is charge-balanced (deficiency is omitted for simplicity), and the semiconducting properties can be expected. But the Sb2−Sb2 distances in $RE_8Sb_{3-\delta}O_8$ are 3.489(1), 3.411(1), and 3.371(1) Å for RE = Sm, Gd, and Ho, and they are much larger than the classical two-center, two-electron Sb−Sb bonds; e.g., the Sb−Sb dimer is 2.82 Å in β-Zn_4Sb_3[35]. Such larger distances imply much weaker Sb−Sb interactions and thus additional—in excess of $2e^-$—electron requirements for the Sb2 atoms in $RE_8Sb_{3-\delta}O_8$.

The LMTO calculations support the metallic behavior of the idealized $Ho_8Sb_3O_8$ structure without Sb2−Sb2 dimers. As expected, the Fermi level sits deep in the valence band, but surprisingly, there is a nonzero DOS between the valence and conduction bands. Analysis of the partial DOS and COHP for individual interactions reveals that the weak Sb2−Sb2 interactions of 3.76 Å are responsible for the disappearance of the band gap. This is rather remarkable, as the Sb2−Sb2 distances are identical to the Sb1−Sb1 ones and the first-nearest-neighbor environments for Sb2 and Sb1 are similar. Currently, we do not fully understand the origin of such behavior, but we believe that the second-nearest-neighbor coordination of Sb2 with fewer O atoms may be responsible for the observed changes. Introducing the Sb2 deficiency of $\delta = 0.046$ in $Ho_8Sb_{3-\delta}O_8$ will raise the Fermi level through decreasing the number of Sb2 states in the valence band, but it will not be sufficient to place the Fermi level at the top of the valence band. Besides, such deficiency—even if large—will not change the nature of electrical conductivity for idealized $Ho_8Sb_3O_8$, as there is no band gap.

Electronic effects of the Sb2−Sb2 dimer formation ($d_{Sb2-Sb2}$ = 3.37 Å) were studied by creating a "superstructure" of $Ho_8Sb_3O_8$ in which the *b* axis was doubled and symmetry was reduced to *P*2 (Figure 3). Due to the shorter Sb2−Sb2 bonds ($d_{Sb2-Sb2}$ = 3.37 vs 3.76 Å), the Sb2 bonding states originating from these bonds dropped in energy, while the antibonding states went up. As a result, the band gap opened between the valence and conduction bands. However, the Fermi level is still deep in the valence band, which suggests that not enough of the Sb2 states were transferred to the higher-energy conduction band. This behavior may not be so surprising, as the Sb2−Sb2 interactions are rather weak. The presence of small Sb2 deficiencies will not change the DOS significantly.

Thus, the DOS calculations point at metallic behavior for $Ho_8Sb_{3-\delta}O_8$; however, the phase is semiconducting. We suggest that semiconducting properties of $Ho_8Sb_{3-\delta}O_8$ as well as of $Sm_8Sb_{3-\delta}O_8$ result from the Anderson-type localization of electrons. According to Anderson, in disordered structures with a nonperiodic potential, the electrons can be localized within the vicinity of a particular atom.[38] Orbitals in such crystals are divided into two types: those in the middle of the band extend through the solid as in a normal crystal, and those close to the top and bottom of the band are localized. The region of localized states in the band will depend on the degree of disorder; in an extreme case all the states may become localized.[39] If the Fermi level lies at the top of the valence band, electrons cannot conduct current well through the solid.[40] It has been suggested that the Anderson mechanism is mainly responsible for metal−insulator transitions in some oxides, such as $La_{1-x}Sr_xVO_3$[41] and

---

(37) Caillat, T.; Fleurial, J. P.; Borshchevsky, A. *J. Phys. Chem. Solids* **1997**, *58*, 1119–1125.

(38) Anderson, P. W. *Phys. Rev.* **1958**, *109*, 1492–1505.

(39) Kramer, B. In *Springer Proceedings on Physics*; Ando, T., Fukuyama, H., Eds.; Springer-Verlag: Berlin/New York, 1988; Vol. 28, p 84.

(40) Cox, P. A. *The Electronic Structure and Chemistry of Solids*; Oxford University Press: Oxford, 1987.

(41) Ganguly, P. C. N. R. In *Localization and Metal−Insulator Transition*; Fritzsche, H., Adler, D., Eds.; Plenum Press: New York/London, 1985; p 53.

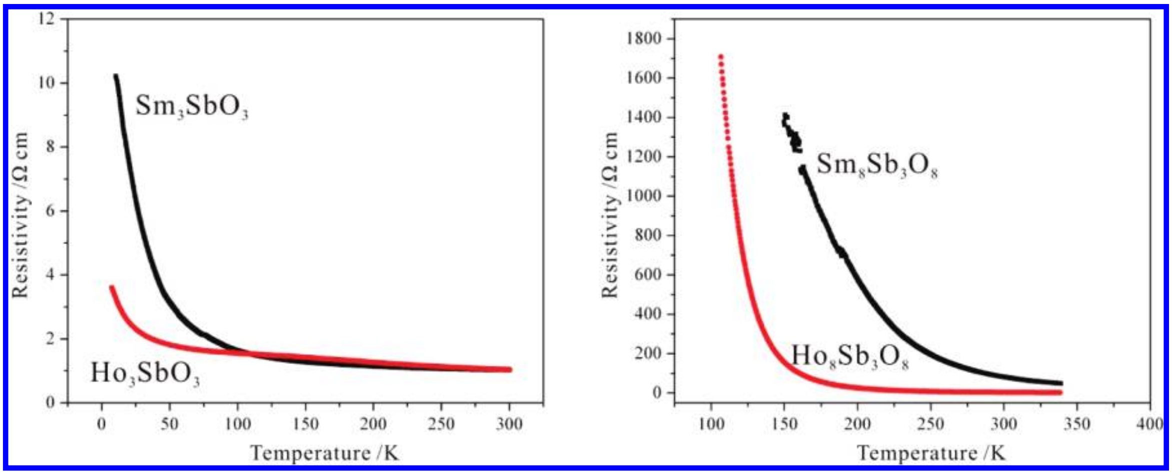

Figure 7. (Left) Electrical resistivity of the Sm_3SbO_3 and Ho_3SbO_3 samples. (Right) Electrical resistivity of the $Sm_8Sb_3O_8$ and $Ho_8Sb_3O_8$ samples.

Table 6. Room-Temperature Electrical Resistivity and Band Gaps for the Sm_3SbO_3, $Sm_8Sb_3O_8$, Ho_3SbO_3, and $Ho_8Sb_3O_8$ Samples

parameter	Sm_3SbO_3	$Sm_8Sb_3O_8$	Ho_3SbO_3	$Ho_8Sb_3O_8$
resistivity/Ω·cm	1.02	86.3	1.05	3.34
band gap/eV	0.0057	0.090	0.011	0.12

$Ba_{1-x}La_xCoO_3$.[42] In the cases of $Ho_8Sb_{3-\delta}O_8$ and $Sm_8Sb_{3-\delta}O_8$, disorder of the Sb2−Sb2 dimers as well as deficiencies on the Sb2 sites can lead to the localized states at the top of the valence band. It worth mentioning that this part of the valence band has significant contributions from the Sb2 orbitals, and thus any loss of the periodicity within the Sb2 sublattice should have a significant impact on electron mobility.

Conclusions

Discovery of the novel RE_3SbO_3 and $RE_8Sb_{3-\delta}O_8$ antimonide oxides was driven by the idea of creating small-band-gap semiconductors by combining semimetallic RESb and insulating RE_2O_3 binaries. This strategy worked for both families of phases as the band gap opened between the valence band, dominated by the Sb states, and the conduction band, composed primarily of the Ho states. For RE_3SbO_3, the Fermi level is at the top of the valence band, and these phases are regular semiconductors. For $RE_8Sb_{3-\delta}O_8$, the Fermi level lies in the valence band due to an insufficient electron count; nevertheless, these phases are semiconducting. The semiconducting behavior of $RE_8Sb_{3-\delta}O_8$ is attributed to the Anderson localization resulting from the random distribution of the Sb−Sb dimers as well as small deficiencies on the Sb site.

Extraordinary thermal stability of the RESb and RE_2O_3 binaries was treated as an indicator that very high temperatures might be required for the synthesis. Indeed, temperatures higher than 1350 °C provided enough energy to overcome the activation barrier between the stable starting materials and products, namely the RE_3SbO_3 and $RE_8Sb_{3-\delta}O_8$ antimonide oxides. We believe that this approach might be applied to other systems.

The compositional and structural similarity of RE_3SbO_3 and $RE_8Sb_{3-\delta}O_8$ appears to control their stability and transformation pathways. In general, the $RE_8Sb_{3-\delta}O_8$ phases are more thermodynamically stable and are final products, regardless of the starting composition. In practice, tuning the temperature and

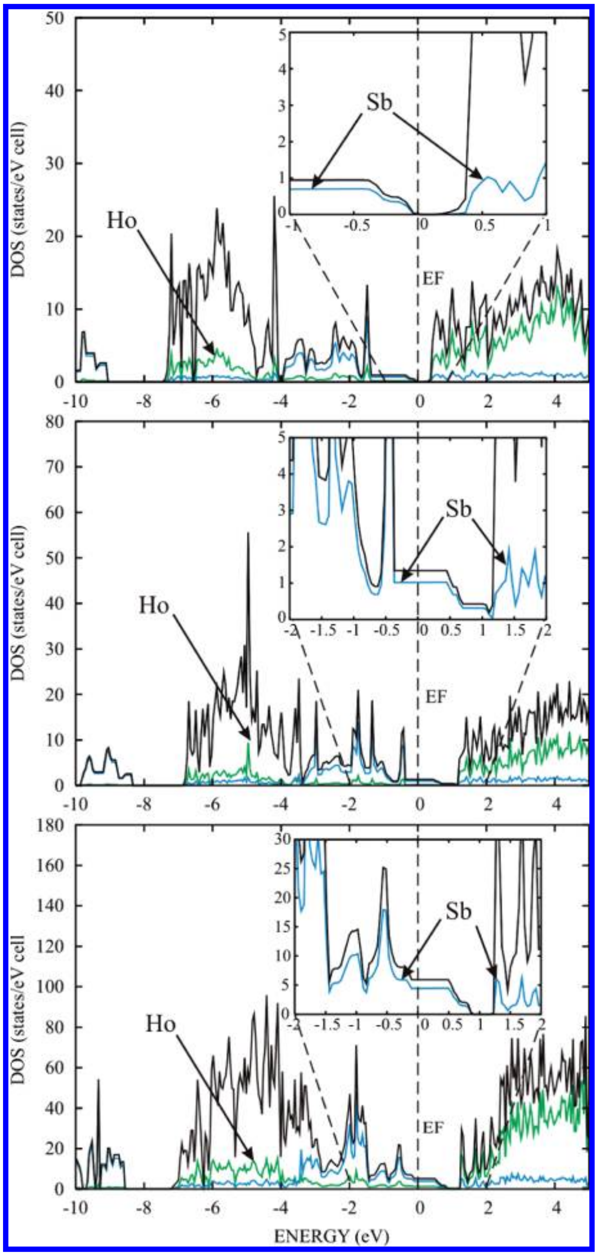

Figure 8. Density of states for RE_3SbO_3 (top), idealized $RE_8Sb_3O_8$ (middle), and the $RE_8Sb_3O_8$ "superstructure" with Sb2−Sb2 dimers (bottom).

---

(42) Yamaura, K.; Cava, R. J. *Solid State Commun.* **2000**, *115*, 301–305.

duration of the heat treatment allows us to obtain selectively either the RE_3SbO_3 or $RE_8Sb_{3-\delta}O_8$ phases.

While we were successful in preparing narrow-band-gap semiconducting antimonide oxides, we failed in making these phases reasonably conductive, which is a requirement for thermoelectric applications.

Acknowledgment. This work was supported by a Discovery Grant from the Natural Sciences and Engineering Research Council of Canada and by a Grant from the ACS Petroleum Research Fund.

Supporting Information Available: Crystallographic data and refinement results for the La_3SbO_3, Sm_3SbO_3, $Sm_8Sb_3O_8$, Gd_3SbO_3, and $Gd_8Sb_3O_8$ single crystals; lattice parameters and phase analysis of the polycrystalline samples; supplementary crystallographic data (CIF). This material is available free of charge via the Internet at http://pubs.acs.org.

JA1027698